

Radio Map Estimation: Empirical Validation and Analysis

Raju Shrestha, Tien Ngoc Ha, Pham Q. Viet, and Daniel Romero

Department of Information and Communication Technology, University of Agder, Norway

{raju.shrestha,tien.n.ha,viet.q.pham,daniel.romero}@uia.no

Abstract—Radio maps quantify magnitudes such as the received signal strength at every location of a geographical region. Although the estimation of radio maps has attracted widespread interest, the vast majority of works rely on simulated data and, therefore, cannot establish the effectiveness and relative performance of existing algorithms in practice. To fill this gap, this paper presents the first comprehensive and rigorous study of radio map estimation (RME) in the real world. The main features of the RME problem are analyzed and the capabilities of existing estimators are compared using large measurement datasets collected in this work. By studying four performance metrics, recent theoretical findings are empirically corroborated and a large number of conclusions are drawn. Remarkably, the estimation error is seen to be reasonably small even with few measurements, which establishes the viability of RME in practice. Besides, from extensive comparisons, it is concluded that estimators based on deep neural networks necessitate large volumes of training data to exhibit a significant advantage over more traditional methods. Combining both types of schemes is seen to result in a novel estimator that features the best performance in most situations. The acquired datasets are made publicly available to enable further studies.

Index Terms—Radio environment map, radio knowledge map, radio map estimation, unmanned aerial vehicles.

I. INTRODUCTION

Radio maps provide a radio frequency (RF) metric at each spatial location of a geographical area [1], [2]. Examples of such metrics include the received signal power, interference power, power spectral density (PSD), electromagnetic absorption, and channel gain. Fig. 1 depicts an example of a power map. Due to their ability to convey information about signal propagation, interference sources, and channel occupancy, radio maps are crucial in many applications, including cellular communications, device-to-device communications, network planning, frequency planning, path planning for autonomous vehicles, dynamic spectrum access, aerial traffic management in unmanned aerial systems, and fingerprinting localization [1]. Radio maps are typically estimated by interpolating measurements acquired across the area of interest.

Most works on radio map estimation (RME) adhere to a common profile: they propose an estimator and compare it with a small number of benchmarks on simulated data; see [1], [3], [4] for a list of references. Thus, the RME literature falls short along two aspects. On the one hand, the RME problem itself is not well understood. Although recent

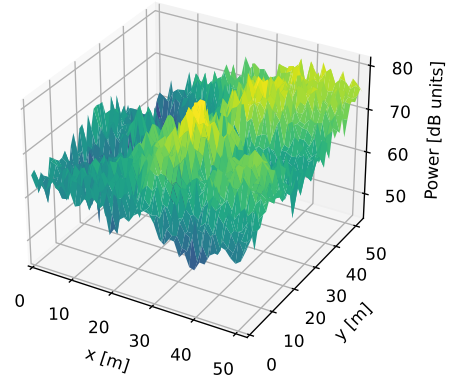


Fig. 1: Power map constructed via grid discretization (Sec. III-B2) of one of the collected measurement sets.

theoretical results offer valuable insight [5], understanding some aspects of the problem require an empirical approach. On the other hand, it is unclear how existing estimators perform and compare in practice. As detailed in Sec. II, the work in this context is still highly limited.

To fill this gap, the following contributions are presented:

- 1) Two large measurement datasets were collected using different technologies. The first comprises received signal strength (RSS) measurements at 198,000 locations with a custom-made system based on a software-defined radio (SDR) on board an unmanned aerial vehicle (UAV) in a band with a central frequency of 918 MHz and bandwidth 2.93 MHz. The second comprises three metrics of several LTE cells collected at 4095 locations by an LTE modem on board a UAV. In both cases, accurate geolocation is obtained by fusing inertial measurements with *real-time kinematics* (RTK) data. To the best of our knowledge, this is also the first work on RME using real data collected by a UAV. Both datasets are published along with this paper.
- 2) The general aspects of the RME problem are empirically investigated. Sec. VI-A lists the main findings. One of the

Relative to the conference version, this paper [6] additionally collects two real datasets: one with significantly more measurements than the conference version, and a new 4G dataset. It conducts comprehensive empirical validation with additional benchmarks, introduces a hybrid estimator that combines a deep neural network (DNN) and multiple traditional estimators, and evaluates the sufficiency of the collected data for training DNNs. Furthermore, all the considered traditional estimators are also trained.

TABLE I: Summary of the main terminology.

Terms	Definition
Dataset	Collection of measurement sets.
Measurement set	Collection of N measurements of a metric corresponding to a given geographical location and transmitter.
Estimation instance	Subset of N out of the N measurements in a measurement set obtained by drawing a patch; cf. Sec. IV.
Set of observed measurements	Subset of N_{obs} measurements or grid points obtained from an estimation instance as described in Sec. V-B.

key theoretical findings in [5], namely that the complexity of the RME problem is larger when the transmitters are close to the mapped region, is corroborated. Besides, the impact of small-scale fading on RME is extensively analyzed and approaches to mitigate its effect are investigated. It is empirically shown that a small root mean-square error (RMSE) can be achieved even with simple estimators for moderate numbers of measurements.

- 3) A representative subset of the radio map estimators in the literature are extensively analyzed and compared using four performance metrics. This includes both traditional estimators as well as estimators based on DNNs. The main findings are listed in Sec. VI-A.
- 4) Inspired by the strengths and limitations of each scheme, a novel estimator is proposed by combining DNN and traditional estimators. This hybrid estimator is seen to outperform all the other estimators in most situations.

The rest of the paper is structured as follows. Sec. II summarizes the related work. Sec. III reviews the RME problem along with some of the most popular estimators in the literature. Sec. IV describes the data collection system and procedure. This data is then used in Sec. V to analyze the performance of the algorithms in Sec. III. Finally, Sec. VI provides a summary of the key findings, a discussion, and the main conclusions.

Terminology. Some terms defined and used throughout the paper are listed in Table I.

II. RELATED WORK

The most related work is [7], where 4 simple interpolators (none based on DNNs) are compared using a single performance metric on a dataset of 1661 measurement locations. Interestingly, it is observed that the performance of the considered estimators does not greatly differ.

Other works with real data are more targeted to assess the performance of a specific estimator. In [8], the RSS of a base station is measured at 700 indoor locations using several types of antennas to evaluate the performance of an algorithm that capitalizes on the transmitter location and a propagation model. In [9], the RSS of multiple WiFi access points is measured at 337 indoor locations and used to compare the performance of the proposed matrix completion algorithm against two benchmarks. In [10], the RSS of 4 WiFi access points is measured at 124 indoor locations to compare the proposed compressed sensing estimator with a basis pursuit and basic model-based path-loss benchmarks. In [11], the RSS of several WiFi access points is measured at 1035 indoor locations to compare their deep learning algorithm with linear regression. In [12], 100 RSS measurements were collected

at outdoor locations to compare their algorithm, which uses the transmitter location, against Kriging, linear regression, and a simulation-based scheme. Even in studies deviating from conventional RME formulations, similar datasets were collected in related problems. For example, in [13], 600 RSS measurements are collected outdoors for various tilt values of the antennas of an LTE base station with the purpose of predicting RSS at all locations for other tilt values. Another related problem is considered in [14], where path loss is predicted using a neural network. Performance is studied with measurements collected at 36,000 locations, but no comparison with other algorithms is carried out. Yet another example, in [15], published before the advent of deep learning, 1238 measurements were collected outdoors and fed to artificial neural networks to predict path loss. The work in [16], which relies on 538 RSS measurements, follows similar lines as [15].

III. RADIO MAP ESTIMATION

Amidst the diverse RME formulations, this section concentrates on the two most prevalent ones, here referred to as the grid-aware and grid-agnostic formulations. To simplify the exposition, it is assumed that the signal strength is quantified using the received signal power, but other metrics will also be considered afterwards.

A. Model

Let $\mathcal{X} \subset \mathbb{R}^2$ encompass the Cartesian coordinates of all points within the region of interest, typically a rectangular area in a horizontal plane. A *power map* is a function that returns the received signal power $\gamma(\mathbf{x})$ for each location $\mathbf{x} \in \mathcal{X}$. This power is the result of the contribution of one or multiple transmitters operating on a given band. For example, if there is a single transmitter with transmit power P_{Tx} , then

$$\gamma(\mathbf{x}) = P_{\text{Tx}} + G - s^{\text{PL}}(\mathbf{x}) - s^{\text{SF}}(\mathbf{x}) - s^{\text{SSF}}(\mathbf{x}), \quad (1)$$

where $s^{\text{PL}}(\mathbf{x})$, $s^{\text{SF}}(\mathbf{x})$, $s^{\text{SSF}}(\mathbf{x})$, and G respectively denote the path loss, the loss due to shadow fading, the loss due to small-scale fading, and the constant gain term that aggregates the gains of the antennas and amplifiers.

The received power is measured by one or multiple receivers (or sensors) with isotropic antennas at N locations $\{\mathbf{x}_n\}_{n=1}^N \subset \mathcal{X}$. The measurement at \mathbf{x}_n can be written as

$$\tilde{\gamma}_n = \gamma(\mathbf{x}_n) + z_n, \quad (2)$$

where z_n represents measurement noise.

B. Problem Formulation

Since the term $s^{\text{SSF}}(\mathbf{x})$ in (2) is caused by multipath, it exhibits a spatial variability at a wavelength scale, which for contemporary communication systems is not generally greater than tens of centimeters. Thus, accurately estimating $s^{\text{SSF}}(\mathbf{x})$ would arguably require a spacing between measurement locations below the wavelength, which would in turn require a prohibitively large number of measurements. For this reason,

it is common in the RME literature to assume that small-scale fading is *averaged out*. Since the impact of such an assumption has never been empirically analyzed, the present work considers two common problem formulations in the literature, one where $s^{\text{SSF}}(\mathbf{x})$ is accounted for and one where $s^{\text{SSF}}(\mathbf{x})$ is averaged out.

1) *Grid-agnostic RME*: In this formulation, small-scale fading is not averaged out. Given N_{obs} observed measurements $\{\mathbf{x}_n, \tilde{\gamma}_n\}_{n=1}^{N_{\text{obs}}}$, the problem is to estimate $\gamma(\mathbf{x})$, $\mathbf{x} \in \mathcal{X}$. In the operational phase, N_{obs} will be set to N . However, for training purposes, it is convenient to split the N acquired measurements into N_{obs} for map estimation and $N - N_{\text{obs}}$ for evaluating the quality of the estimate. Although the above notation indicates that the observed measurements are the first N_{obs} measurements, this is not necessary. In fact, the observed measurements can be any subset of the N measurements.

2) *Grid-aware RME*: The second formulation adopts a *grid discretization* approach, indirectly mitigating the effects of small-scale fading. This method is commonly employed by numerous existing estimators, including those based on deep learning, compressed sensing, and matrix completion. Consider an $N_y \times N_x$ rectangular grid $\mathcal{G} = \{\mathbf{x}_{i,j}^{\mathcal{G}}, i = 1, \dots, N_y, j = 1, \dots, N_x\} \subset \mathcal{X}$, where $\mathbf{x}_{i,j}^{\mathcal{G}} = [\Delta(N_y - i), \Delta(j - 1)]^T$ and Δ is the grid spacing. This assignment facilitates identifying the grid with a matrix. For each n , the measurement at \mathbf{x}_n is assigned to the nearest grid point. Subsequently, all measurements assigned to the (i, j) -th grid point are averaged to obtain $\tilde{\gamma}_{i,j}$. The resulting measurements are then arranged in the matrix $\tilde{\Gamma} \in \mathbb{R}^{N_y \times N_x}$, whose (i, j) -th entry equals $\tilde{\gamma}_{i,j}$ if at least one measurement has been assigned to $\mathbf{x}_{i,j}^{\mathcal{G}}$ and an arbitrary value (e.g. 0) otherwise. It is also convenient to form the *mask* $\mathbf{S} \in \{0, 1\}^{N_y \times N_x}$, which is an $N_y \times N_x$ matrix whose (i, j) -th entry equals 1 if at least one measurement has been assigned to $\mathbf{x}_{i,j}^{\mathcal{G}}$ and 0 otherwise. Since $\tilde{\gamma}_{i,j}$ is the average of measurements acquired typically several wavelengths away, the contribution of $s^{\text{SSF}}(\mathbf{x})$ is significantly reduced. The remaining terms in (1) evolve more slowly across space and, therefore, they do not vanish upon averaging.

Given $\tilde{\Gamma}$ and \mathbf{S} , the problem is to estimate the power map without the small-scale fading contribution for all $\mathbf{x} \in \mathcal{G}$. In the example of (1), this can be expressed as

$$\gamma_{\text{NSSF}}(\mathbf{x}) := P_{\text{Tx}} + G - s^{\text{PL}}(\mathbf{x}) - s^{\text{SF}}(\mathbf{x}). \quad (3)$$

C. Radio Map Estimators

The estimators considered in this work are outlined next. Implementation details are deferred to Sec. V.

1) *K-Nearest Neighbors (K-NN)*: This algorithm simply averages the measurements collected at the K locations with the smallest distance to the evaluation point. Specifically, given \mathbf{x} , let $\nu_k(\mathbf{x})$ denote the index of the k -th nearest point among $\{\mathbf{x}_n\}_{n=1}^{N_{\text{obs}}}$. For example, $\nu_1(\mathbf{x}) = \arg \min_n \|\mathbf{x}_n - \mathbf{x}\|$ whereas $\nu_{N_{\text{obs}}}(\mathbf{x}) = \arg \max_n \|\mathbf{x}_n - \mathbf{x}\|$. Although many variants exist, the simplest is to obtain $\hat{\gamma}(\mathbf{x}) = (1/K) \sum_{k=1}^K \tilde{\gamma}_{\nu_k(\mathbf{x})}$.

2) *Kriging*: This (see e.g. [17]) is a common spatial interpolation technique extensively applied to RME [2], [18]–[20]. In *simple kriging*, $\gamma(\mathbf{x})$ is modeled for each \mathbf{x} as a random variable whose spatial mean $\mu_{\gamma}(\mathbf{x}) := \mathbb{E}[\gamma(\mathbf{x})]$ and covariance

$\text{Cov}[\gamma(\mathbf{x}), \gamma(\mathbf{x}')] are known for all \mathbf{x} and \mathbf{x}' . In practice, these functions are estimated from data. Under model (2), assume that z_n is zero-mean with variance σ_z^2 and uncorrelated with $z_{n'}$ for all $n' \neq n$ and with $\gamma(\mathbf{x})$ for all \mathbf{x} . Thus, the mean and covariance of the measurements are respectively $\mathbb{E}[\tilde{\gamma}_n] = \mu_{\gamma}(\mathbf{x}_n)$ and $\text{Cov}[\tilde{\gamma}_n, \tilde{\gamma}_{n'}] = \text{Cov}[\gamma(\mathbf{x}_n), \gamma(\mathbf{x}_{n'})] + \sigma_z^2 \delta_{n,n'}$, where $\delta_{n,n'}$ equals 1 if $n = n'$ and 0 otherwise. It can also be verified that $\text{Cov}[\gamma(\mathbf{x}), \tilde{\gamma}_n] = \text{Cov}[\gamma(\mathbf{x}), \gamma(\mathbf{x}_n)]$. The simple kriging estimate is nothing but the linear minimum mean square error (LMMSE) estimator of $\gamma(\mathbf{x})$ based on the measurements $\tilde{\gamma} := [\tilde{\gamma}_1, \dots, \tilde{\gamma}_{N_{\text{obs}}}]^T$:$

$$\hat{\gamma}(\mathbf{x}) = \mu_{\gamma}(\mathbf{x}) + \text{Cov}[\gamma(\mathbf{x}), \tilde{\gamma}] \text{Cov}^{-1}[\tilde{\gamma}, \tilde{\gamma}] (\tilde{\gamma} - \mathbb{E}[\tilde{\gamma}]), \quad (4)$$

where $\text{Cov}[\tilde{\gamma}, \tilde{\gamma}]$ is the $N_{\text{obs}} \times N_{\text{obs}}$ matrix whose (n, n') -th entry is $\text{Cov}[\tilde{\gamma}_n, \tilde{\gamma}_{n'}]$ and $\text{Cov}[\gamma(\mathbf{x}), \tilde{\gamma}]$ is the $1 \times N_{\text{obs}}$ vector whose n -th entry equals $\text{Cov}[\gamma(\mathbf{x}), \tilde{\gamma}_n]$.

3) *Kernel-based Learning*: Kernel-based estimators, grounded in the theory of reproducing-kernel Hilbert spaces [21], are also common in RME; see [22] and references therein. They return estimates of the form $\hat{\gamma}(\mathbf{x}) = \sum_{n=1}^{N_{\text{obs}}} \alpha_n \kappa(\mathbf{x}, \mathbf{x}_n)$, where the coefficients α_n depend on the specific estimator and κ is a user-selected symmetric positive (semi)definite function called kernel. A common example of kernel function is the so-called Gaussian radial basis function of width $s > 0$, namely $\kappa(\mathbf{x}, \mathbf{x}') := \exp\{-\|\mathbf{x} - \mathbf{x}'\|^2/s\}$. One of the simplest estimators is *kernel ridge regression (KRR)*, where $\{\alpha_n\}_{n=1}^{N_{\text{obs}}}$ can be obtained in closed form by solving

$$\underset{\{\alpha_n\}_{n=1}^{N_{\text{obs}}}}{\text{minimize}} \frac{1}{N_{\text{obs}}} \sum_{n=1}^{N_{\text{obs}}} \left| \tilde{\gamma}_n - \sum_{n'=1}^{N_{\text{obs}}} \alpha_{n'} \kappa(\mathbf{x}_n, \mathbf{x}_{n'}) \right|^2 + \rho \sum_{n=1}^{N_{\text{obs}}} \alpha_n^2. \quad (5)$$

4) *Deep Learning*: Numerous estimators leveraging DNNs have been proposed [11]–[13], [19], [23]–[30] for RME. A typical approach is to concatenate $\tilde{\Gamma}$ and \mathbf{S} to form a $2 \times N_y \times N_x$ tensor that is passed as an input to a neural network, which returns an $N_y \times N_x$ matrix $\hat{\Gamma}$ whose (i, j) -th entry is an estimate for $\gamma_{\text{NSSF}}(\mathbf{x}_{i,j}^{\mathcal{G}})$. To simplify subsequent expressions, this estimate will still be denoted as $\hat{\gamma}(\mathbf{x}_{i,j}^{\mathcal{G}})$.

IV. DATA COLLECTION AND PREPARATION

To train and test the radio map estimators, it is necessary to generate a large number of *estimation instances*, each one comprising N measurements in an area \mathcal{X} ; cf. Sec. III-B. For specificity, \mathcal{X} is assumed to be a rectangle $\mathcal{X} = [0, L_y] \times [0, L_x]$, where L_y and L_x are respectively the side lengths in the y and x directions. A naïve approach would be to separately acquire sets of N measurements, each one in a different $L_y \times L_x$ geographical location. However, this requires collecting a very large number of measurements. Instead, a more efficient approach is to collect a large number \underline{N} of measurements in a large rectangle $\underline{\mathcal{X}} = [0, \underline{L}_y] \times [0, \underline{L}_x]$, where $\underline{L}_y \gg L_y$ and $\underline{L}_x \gg L_x$. The set of these \underline{N} measurements will be referred to as a *measurement set*; cf. Table I. Then, a large number of estimation instances can be generated by forming $L_y \times L_x$ rectangular patches inside $\underline{\mathcal{X}}$ and selecting the measurements inside each patch.

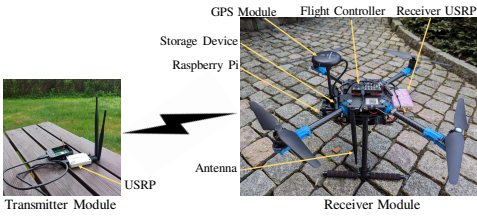


Fig. 2: Transmitter and receiver and modules.

As will become clear, to study grid-aware estimators and the impact of small-scale fading it is useful that the measurements in a patch are aligned to some extent with the grid; cf. Sec. III-B2. To accommodate this need, an $\underline{N}_y \times \underline{N}_x$ grid with spacing Δ is defined on \mathcal{X} , meaning that $\underline{L}_x = \underline{N}_x \Delta$ and $\underline{L}_y = \underline{N}_y \Delta$. To ensure that the measurements in each patch remain aligned with the grid, the patches are formed by randomly drawing the location of the bottom-left corner such that its x and y -coordinates are integer multiples of Δ . This yields at most $(\underline{N}_x - N_x + 1)(\underline{N}_y - N_y + 1)$ distinct patches.

The rest of the section details the procedures to collect the measurement sets, which are grouped into two datasets.

A. USRP Dataset

The first dataset comprises 18 measurement sets and was collected using a transmitter stationed at a fixed ground location and a receiver mounted on a UAV.

1) *Transmitter*: The transmitter (see Fig. 2) is a Universal Software Radio Peripheral (USRP) B205 mini-i operated by a Raspberry Pi, both of which are connected through a battery elimination circuit (BEC) to a battery so that they can be deployed on the field. The antenna is a 21 cm-long monopole with an operating range of 824-960 MHz and 1710-1990 MHz. The USRP transmits an *orthogonal frequency-division multiplexing* (OFDM) signal with 1024 subcarriers, and sampling rate of 5 MHz, which yields a subcarrier spacing of 15 KHz. The 600 central subcarriers are modulated with QPSK symbols that encode a pseudo-random bit sequence. The remaining subcarriers are unused, which yields an effective bandwidth of roughly $600/1024 \cdot 5 \text{ Mhz} \approx 2.93 \text{ MHz}$. The cyclic prefix is of length 256. A frame that contains 12 OFDM symbols is repeatedly transmitted with a carrier frequency of 918 MHz. This band is mostly unused in Norway.

2) *Receiver*: The receiver, which is a USRP B205 mini-i with the same antenna as the transmitter (Fig. 2), is installed on a quadcopter with a Raspberry Pi companion computer. The quadcopter was assembled using a Holybro X500 v2 frame and a Pixhawk 4 flight controller (FC) that runs a PX4 autopilot. The autopilot estimates the vehicle location by fusing the measurements of an *inertial measurement unit* (IMU) and an RTK module, resulting in an accuracy of around 30 cm.

Every second, the receiver module captures approximately 15 uniformly-spaced blocks of 100,000 samples. Given that the speed is 4 m/s, the average distance between sample blocks is around 27 cm, slightly smaller than the wavelength of the transmission. This is useful to average out small-scale fading, as described in Sec. III-B. Together with each sample block, the receiver stores the corresponding location estimate.

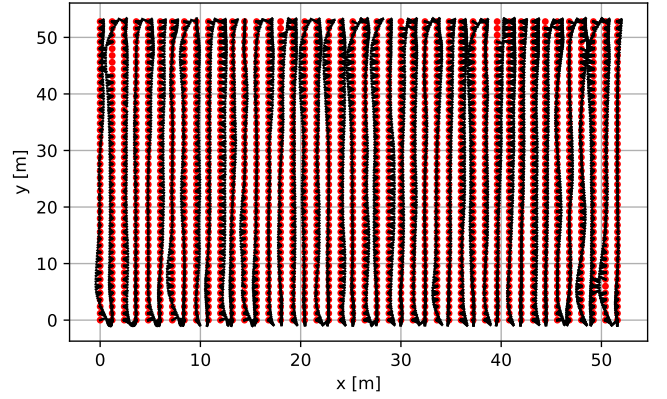


Fig. 3: Grid quantization (cf. Sec. III-B2) of the measurement locations in one of the collected measurement sets in the USRP dataset. Red dots denote grid points and small black lines connect each measurement location to its nearest grid point.

The sample blocks are processed offline with an algorithm designed for this project to coherently estimate the received signal power, which requires accurate synchronization but minimizes measurement error due to noise and interference.

3) *Data Collection Procedure and Postprocessing*: For safety reasons, data was collected in a flat agricultural terrain away from residential areas. The transmitter is placed about 50 cm above the ground. To shape different shadow fading patterns, metallic reflectors were arranged around the transmitter in a different configuration for each of the 18 measurement sets. In each of them, \underline{N} is approximately 11,000.

To facilitate experiments with grid quantization, the UAV follows a trajectory with a height of 7 m that comprises parallel lines spaced by Δ . Fig. 3 illustrates this trajectory for one of the measurement sets after removing the turnarounds. To minimize changes in the channel due to the UAV frame, the yaw angle is kept constant. To maximize the number of patches, the region was selected such that $\underline{N}_x = \underline{N}_y$; cf. the beginning of Sec. IV. The size of the region is limited by the battery life of the UAV. With the adopted configuration, the UAV can fly for about 10 minutes. With a speed of 4 m/s, this means that a distance of 2400 m can be covered. If one wishes to allow for the creation of a grid with $\underline{N}_x = \underline{N}_y$ and spacing Δ , the UAV must travel a distance of $(\underline{N}_x + 1)\underline{N}_x \Delta$. Therefore, Δ and \underline{N}_x must be selected such that $(\underline{N}_x + 1)\underline{N}_x \Delta = 2400$. Given that $\underline{L}_x = \underline{N}_x \Delta$, there is a trade-off between the number of patches (determined by \underline{N}_x) and the size of the region. To attain a reasonable value for both quantities, \underline{N}_x was set to 44, which yields $\Delta \approx 1.2 \text{ m}$.

Each measurement set is then cleaned to keep only a subset of the measurements that lie inside a rectangular region, which removes the turnaround parts of the trajectory as well as the path from the take-off location to the first waypoint and from the last waypoint to the landing location.

The geodetic coordinates stored by the receiver are then converted to Cartesian coordinates and the latter are translated and rotated so that the measurement locations align as much as possible with the grid. This means that most grid points should

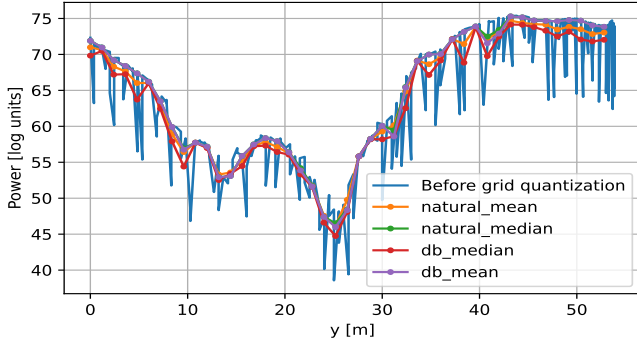


Fig. 4: Measurements in the 41-th column of Fig. 3 vs. the y -coordinate of their location. Orange, Green, Red, Purple: Measurements $\{\tilde{\gamma}_{i,j}\}_j$ for a fixed $j = 41$ vs. the y -coordinate of $\mathbf{x}_{i,j}^G$, with grid quantization modes natural mean, dB mean, natural median, and dB median respectively. Blue: measurements $\{\tilde{\gamma}_n\}_n$ assigned to the points in $\{\mathbf{x}_{i,j}^G\}_j$.

be assigned to at least one measurement location. However, due to the effects of wind or the UAV momentum when changing direction, some of the grid points may not be assigned to any measurement; cf. Fig. 3. Yet, the alignment is sufficiently good to allow the visualization of each measurement set as in Fig. 1, where just the grid quantization procedure from Sec. III-B was applied. Observe that the ripple effect of small-scale fading (cf. $s^{\text{SSF}}(\mathbf{x})$ in (1)) has not been totally suppressed as a result of grid quantization.

To entirely mitigate this effect, one could adopt a larger grid spacing Δ , but this would come at the cost of reduced spatial resolution. Another possibility is to consider alternative functions for combining the measurements assigned to each grid point; cf. Sec. III-B2. To this end, Fig. 4, illustrates the measurements assigned to the grid points in a column of Fig. 3 before and after grid quantization using various combination functions. Specifically, $\tilde{\gamma}_{i,j}$ is obtained by taking the mean or median of the measurements assigned to $\mathbf{x}_{i,j}^G$, either in natural or dB units. It is observed that averaging the measurements in dB units leads to the best averaging of small-scale fading. For this reason, this is the approach adopted in the rest of the paper. Yet, although this is the most effective of the considered alternatives, its effectiveness is limited, as this was already the function used in Fig. 3. This calls for further research on the development of more effective combining functions.

B. 4G Dataset

The second dataset is intended to assess RME in cellular setups. It comprises a large number of measurement sets, each one for a different metric and 4G cell in two geographical areas. The reason for focusing on 4G systems is their wider coverage relative to their 5G counterparts, especially away from urban areas, where UAVs are allowed to fly.

1) *Transmitter*: The transmitters are the base stations deployed by a cellular operator in a real-world 4G network.

2) *Receiver*: The receiver is a Quectel RM510Q-GL modem on board a DJI Matrice 300 RTK UAV. The localization

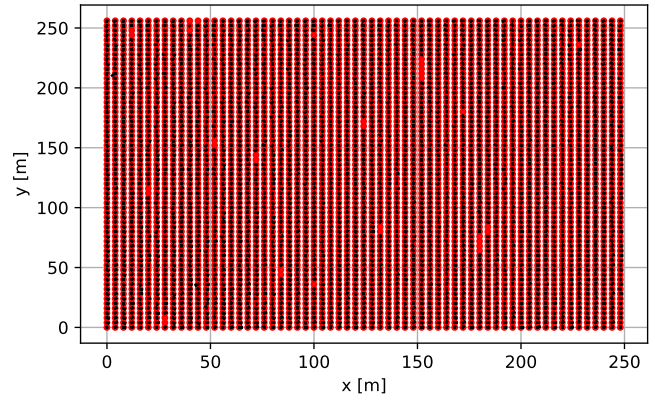


Fig. 5: Grid quantization of the measurement locations in one of the collected measurement sets of the 4G dataset. Red dots denote grid points and small black lines connect each measurement location to its nearest grid point.

module is the built-in RTK rover module of the UAV, which ensures highly accurate geo-referencing of the LTE data.

The magnitudes measured at each location comprise the *reference signal received power* (RSRP), the *received signal strength indicator* (RSSI), and the *reference signal received quality* (RSRQ) for the serving cell as well as for 8 neighboring cells. These metrics are measured and stored on board together with the location estimates.

3) *Data Collection Procedure and Postprocessing*: The data is collected in two remote areas away from agricultural and residential facilities. In both cases, $L_x = 252$ m and $L_y = 260$ m and the height is 20 m. A rectangular grid with $\Delta = 4$ m is constructed and the UAV hovers at each grid point to collect 5 measurements per metric. 93 cells are measured at least at one point for the first area and 31 for the second one. The measurement locations are rotated and translated to maximize the alignment with the grid; cf. Fig. 5.

V. EXPERIMENTS WITH REAL DATA

In this section, the collected data is utilized to test eight radio map estimators. Table I summarizes the main terminology.

For training and for conducting Monte Carlo (MC) experiments, estimation instances are generated by drawing “patches” in the region \mathcal{X} of a measurement dataset selected uniformly at random as detailed at the beginning of Sec. IV. The resulting measurements are denoted as $\{(\mathbf{x}_n, \tilde{\gamma}_n)\}_{n=1}^N$. Thus, \mathbf{x}_n , $\tilde{\gamma}_n$, and N should be thought of as random variables that take new values for each patch or MC iteration. For simplicity, patches are square, which means that $L_x = L_y := L$.

Before delving into MC experiments, Fig. 6 illustrates an example of map estimation for a randomly selected patch of approximately 1,475 m² using the USRP data set; see Sec. V-C. The number of observations $N_{\text{obs}} = 120$, marked as black crosses, was selected so that all estimates are of a reasonable quality.

A. Compared Algorithms

The compared algorithms include:

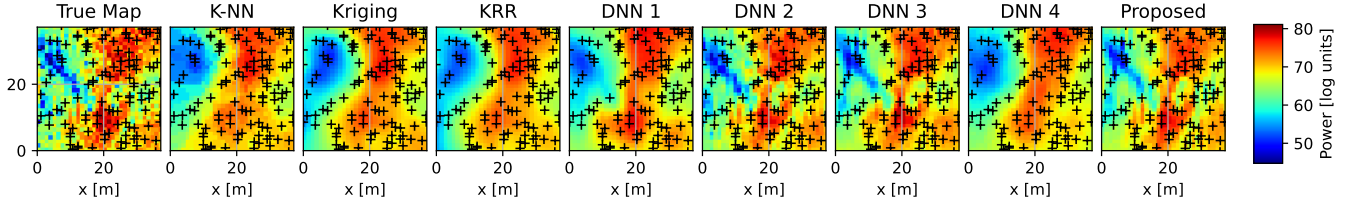


Fig. 6: True map and map estimates produced by the considered map estimators for an estimation instance part of the USRP dataset when $L = 38.4$ m, $\Delta = 1.2$, and $N_{\text{obs}} = 120$. Black crosses denote measurement locations.

1) *Non-DNN Estimators*: Three non-DNN estimators or traditional estimators are considered, namely K-NN, simple Kriging, and KRR; cf. Sec. III-C. The parameters of these estimators are obtained via exhaustive search over a grid of candidate values by minimizing a sample estimate of the RMSE (6) on the training estimation instances of the corresponding experiment. The range of possible values was set to include the optimal value in its interior. The specifics of each algorithm are detailed next.

- 1) K-NN is trained for $K \in [2, 3, \dots, 13]$.
- 2) Simple Kriging adopts the correlated shadow fading model from [31]. This model can be defined by $\mathbb{E}[\gamma(\mathbf{x})] = 0$ and $\text{Cov}(s^{\text{SF}}(\mathbf{x}), s^{\text{SF}}(\mathbf{x}')) = \sigma_s^2 2^{-\|\mathbf{x} - \mathbf{x}'\|/\delta_s}$, where σ_s^2 captures variability and δ_s is the distance at which the correlation decays to $1/2$; see [19] for details. The values used for training are $\sigma_s^2 \in [0.01^2, 0.11^2, \dots, 0.91^2]$ and $\delta_s \in [50, 100, \dots, 600]$ m.
- 3) KRR is trained for all combinations of $\rho \in [10^{-12}, 10^{-11}, \dots, 10^{-1}]$ and kernels in a set that includes both Gaussian and Laplacian kernels of width $s \in [20, 30, \dots, 150]$.

2) *DNN Estimators*: Four DNN estimators from the literature were considered. They construct a grid with $N_x = N_y = L/\Delta$ and obtain $\tilde{\Gamma}$ and \mathbf{S} as described in Sec. III-B2. A forward pass yields $\hat{\Gamma}$, which provides estimates of the map at the grid locations. Estimates off the grid points are obtained as the entry of $\hat{\Gamma}$ corresponding to the nearest grid point. To generate training input-output pairs, $\tilde{\Gamma}$ and \mathbf{S} are first obtained from all the N measurements in a patch. The input is then obtained by setting a randomly selected subset of entries of both $\tilde{\Gamma}$ and \mathbf{S} equal to 0, leaving just N_{obs} non-zero entries; see details in Sec. V-B2. The targets are the complete $\tilde{\Gamma}$.

The DNNs were implemented in TensorFlow and trained with the Adam optimizer with a constant learning rate of 10^{-4} and batch size of 200. All DNN-based estimators use convolutional DNNs and they mainly differ in their architectures.

- 1) DNN 1 is the network in [19], which has an autoencoder architecture with 60 M trainable parameters. This is the network with the highest complexity among the ones considered here.
- 2) DNN 2 is the U-Net from [28]. Four layers were removed, as was required to accommodate the grid size used here. With 9 M trainable parameters in total, it features the second highest complexity.
- 3) DNN 3 follows the U-Net architecture in [25] with 20

layers but with *leaky ReLU* activations, since the original tanh activation resulted in poor performance. With 4.6 M trainable parameters, it has the third highest complexity.

- 4) DNN 4 is the completion autoencoder from [24]. With 142 K trainable parameters, it has the lowest complexity.

3) *Proposed Hybrid Estimator*: To benefit from the strengths of both kinds of estimators, a hybrid estimator that combines DNN and non-DNN estimators is proposed here. In particular, three estimates of the map on the grid are obtained using the three estimators in Sec. V-A1 and concatenated to $\tilde{\Gamma}$ and \mathbf{S} to form a $5 \times N_y \times N_x$ tensor. This is passed as the input to a neural network, which produces the $N_y \times N_x$ estimate $\hat{\Gamma}$. The architecture is the same as DNN 3. The values of the parameters of the non-DNN estimators are the ones obtained by training each of them separately; see Sec. V-A1.

B. Performance Metrics

To assess performance in a variety of scenarios that reflect the relevant aspects of the main applications of RME, this section introduces four different metrics.

1) *Grid-agnostic Estimation*: When solving the problem in Sec. III-B1, it is natural to quantify performance by the estimation error at the locations of unobserved measurements, not necessarily on a grid. Specifically, at each MC iteration, $\mathcal{M} := \{(\mathbf{x}_n, \tilde{\gamma}_n)\}_{n=1}^N$ is split into two subsets by partitioning the index set $\mathcal{N} := \{1, 2, \dots, N\}$ into \mathcal{N}_{obs} and $\mathcal{N}_{\text{nobs}}$, that is, $\mathcal{N}_{\text{obs}} \cup \mathcal{N}_{\text{nobs}} = \mathcal{N}$ and $\mathcal{N}_{\text{obs}} \cap \mathcal{N}_{\text{nobs}} = \emptyset$. The cardinality $N_{\text{obs}} := |\mathcal{N}_{\text{obs}}|$ is fixed. The measurements with index in \mathcal{N}_{obs} are passed to each estimator and the returned map estimate $\hat{\gamma}(\mathbf{x})$ is evaluated at the locations $\{\mathbf{x}_n\}_{n \in \mathcal{N}_{\text{nobs}}}$. The RMSE can then be defined as

$$\text{RMSE} := \sqrt{\frac{1}{|\mathcal{N}_{\text{nobs}}|} \mathbb{E} \left[\sum_{n \in \mathcal{N}_{\text{nobs}}} |\tilde{\gamma}_n - \hat{\gamma}(\mathbf{x}_n)|^2 \right]}, \quad (6)$$

where the expectation \mathbb{E} is over patches and index sets \mathcal{N}_{obs} sampled uniformly at random without replacement from \mathcal{N} .

However, this sampling approach may not capture the clustered nature of measurement locations in certain applications. This situation arises e.g. when a cellular device collects numerous measurements in a small part of \mathcal{X} where its user is located, but no measurements are taken where the user is absent during the acquisition stage. To capture this effect, define the metric RMSE_G as in (6) but with a different distribution for \mathcal{N}_{obs} : After creating a rectangular grid with spacing Δ , each

measurement location is assigned to the nearest grid point. Then N_{obs} grid points are selected uniformly at random and \mathcal{N}_{obs} is formed by collecting the indices of the measurements assigned to the selected grid points. Note that in this case N_{obs} no longer indicates the number of observed measurements, but the number of measurement clusters.

2) *Grid-aware Estimation*: When solving the problem in Sec. III-B2, it is natural to evaluate the performance on \mathcal{G} . To this end, at each MC iteration, $\tilde{\mathbf{I}}$ and \mathbf{S} are constructed as in Sec. III-B2. Let $\mathcal{N} \subset \{1, \dots, N_y\} \times \{1, \dots, N_x\}$ denote the set of pairs (i, j) such that $[\mathbf{S}]_{i,j} = 1$. As before, \mathcal{N} is partitioned into \mathcal{N}_{obs} and $\mathcal{N}_{\text{nobs}}$, where $|\mathcal{N}_{\text{obs}}|$ is given. To simplify the exposition, the symbol N_{obs} will be used here to denote $|\mathcal{N}_{\text{obs}}|$. Each estimator receives \mathcal{N}_{obs} and $\{\tilde{\gamma}_{i,j}\}_{(i,j) \in \mathcal{N}_{\text{obs}}}$ and produces an estimate $\hat{\Gamma}$. To quantify performance, consider

$$\text{RMSE}_{\text{G-nobs}} := \sqrt{\frac{1}{|\mathcal{N}_{\text{nobs}}|} \mathbb{E} \left[\sum_{(i,j) \in \mathcal{N}_{\text{nobs}}} |\tilde{\gamma}_{i,j} - \hat{\gamma}(\mathbf{x}_{i,j})|^2 \right]}, \quad (7)$$

where \mathbb{E} is over patches and over \mathcal{N}_{obs} , which is drawn uniformly at random over \mathcal{N} without replacement.

Various estimators may place different emphasis on the spatial smoothness of their estimates. Thus, it is also insightful to consider $\text{RMSE}_{\text{G-all}}$, where \mathcal{N}_{obs} is drawn in the same way as in $\text{RMSE}_{\text{G-nobs}}$ but the evaluation takes place at all grid points in \mathcal{N} , that is, $\mathcal{N}_{\text{nobs}}$ in (7) is replaced with \mathcal{N} . Note that $\text{RMSE}_{\text{G-all}}$ is the typical metric used for training DNN-based estimators in the RME literature.

C. Monte Carlo Experiments with USRP Data

The metrics in Sec. V-B are obtained next using MC experiments. In the case of USRP data, 16 out of the collected 18 measurement sets are used for training and the remaining 2 for testing. A total of 40,000 estimation instances are formed by first choosing a training measurement dataset uniformly at random and then randomly choosing a patch; cf. Sec. IV. Each of these estimation instances is partitioned into an observed and an unobserved set 5 times as described in Sec. V-B2, resulting in a total of 200,000 training examples.

Figs. 7 and 8 depict all four performance metrics when the patch side is $L = 19.2$ m, which results in an area of 369 m^2 and $N_x = N_y = L/\Delta = 16$. This value of L ensures that the test set contains a sufficiently high number of distinct patches and the training set is sufficiently rich for DNN training. To generate each training example, N_{obs} was drawn uniformly at random between 10 and 100.

Overall, the error of most estimators for a sufficiently large N_{obs} is around 5 dB for the grid-agnostic metrics and 3 dB for the grid-aware metrics. This agrees with intuition: grid metrics rely on grid quantization, which averages out small-scale fading. This reduces the spatial variability of the target $\gamma(\mathbf{x})$, which renders it an easier function to estimate. Within grid-agnostic metrics, it is observed in Fig. 7 that RMSE_{G} is generally smaller than RMSE . The reason is that the fact that the measurement locations are more clustered for RMSE_{G}

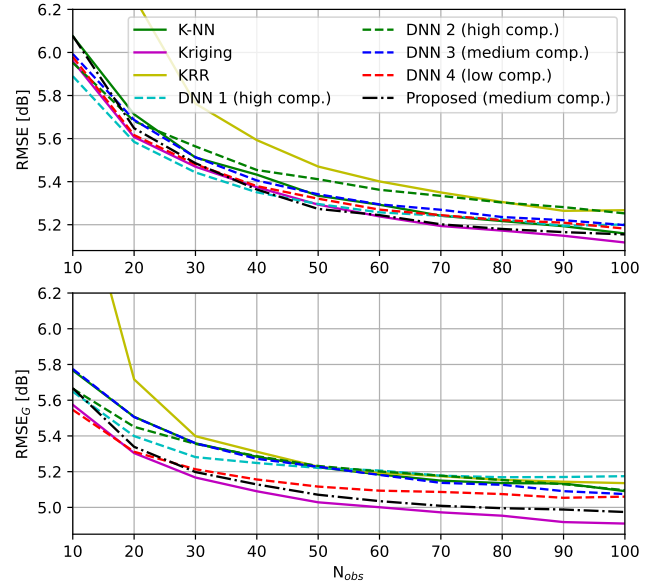


Fig. 7: Grid-agnostic performance metrics for USRP data vs. the number of observations when $L = 19.2$ m, $\Delta = 1.2$, and the estimators are trained with $N_{\text{obs}} \in [10, 100]$.

encourages estimators to fit a local average of the measurements in each cluster rather than each measurement separately. This results in an implicit averaging of measurement noise and small-scale fading, which leads to spatially smoother estimates. Observe that the best estimators approximately attain their minimum RMSE_{G} with 60 observations, which amounts to one observation for every 6.1 m^2 .

Regarding grid-aware metrics, note from Fig. 8 that $\text{RMSE}_{\text{G-nobs}}$ is generally higher than $\text{RMSE}_{\text{G-all}}$. This is expected as the grid points where $\text{RMSE}_{\text{G-all}}$ is evaluated includes the grid points where measurements have been observed. In fact, as N_{obs} increases, the $\text{RMSE}_{\text{G-all}}$ of any reasonable estimator will continue decreasing until N_{obs} reaches $|\mathcal{N}|$. At this point, even the trivial estimator that returns $\hat{\gamma}(\mathbf{x}_{i,j}^{\mathcal{G}}) = \tilde{\gamma}_{i,j}$ for all i, j will attain $\text{RMSE}_{\text{G-all}} = 0$.

Remarkably, the differences across algorithms are not very large. For grid-agnostic metrics, the difference between the best and worst algorithm is around 0.2 dB, whereas for grid-aware metrics, this difference is around 1 dB. Simple algorithms such as K -NN and Kriging offer highly competitive performance relative to pure DNN estimators. Thus, depending on the application, using DNN estimators may not be worth given their need for training on a large data set. The proposed hybrid algorithm is designed to yield good performance in the absence of a large training data set and an even better performance is attained if such data is available. Indeed, it is seen in Fig. 7 that it features the best grid-aware metrics. Note, however, that this algorithm need not result in the best values for all metrics since it is trained specifically for $\text{RMSE}_{\text{G-all}}$.

Each algorithm uses the same parameters (in the case of the DNN estimators, this comprises the weights and biases) for all values of N_{obs} in Figs. 7 and 8. Thus, improved performance must be expected if these parameters are allowed to take

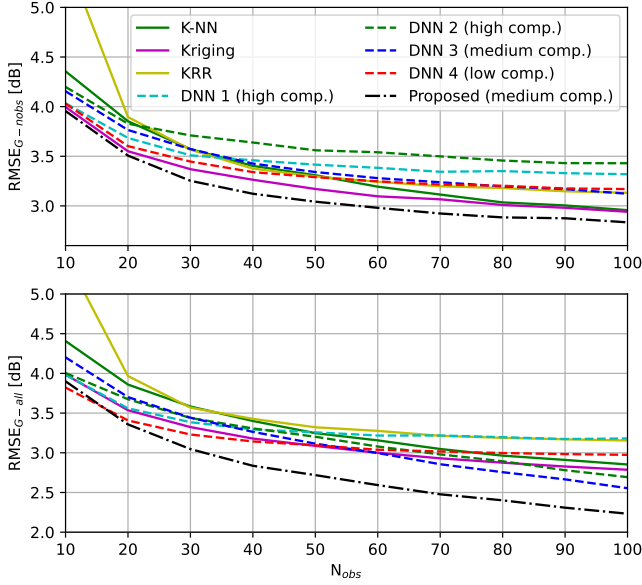


Fig. 8: Grid-aware performance metrics for USRP data vs. the number of observations when $L = 19.2$ m, $\Delta = 1.2$, and the estimators are trained with $N_{\text{obs}} \in [10, 100]$.

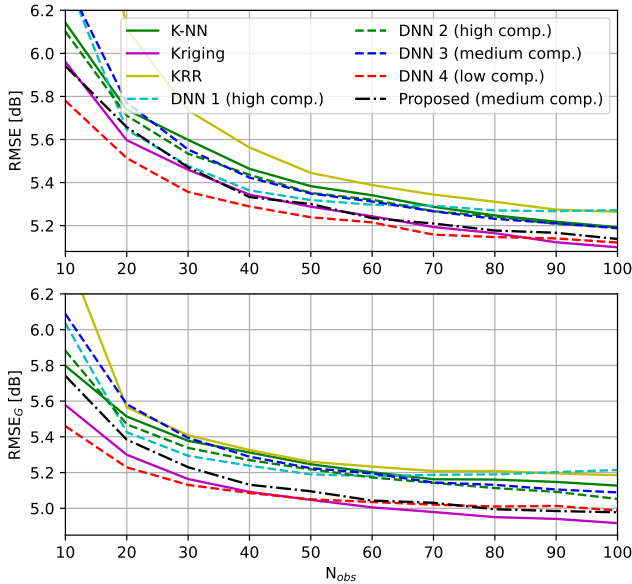


Fig. 9: Grid-agnostic performance metrics for USRP data vs. the number of observations when $L = 19.2$ m, $\Delta = 1.2$, and the estimators are trained with $N_{\text{obs}} = 50$. The weights of the DNNs are initialized with the weights obtained from training the DNNs with $N_{\text{obs}} \in [10, 100]$.

different values depending on N_{obs} . To investigate this effect, Figs. 9 and 10 present the same metrics as in Figs. 7 and 8 after training the estimators for $N_{\text{obs}} = 50$. As in Figs. 7 and 8, the x-axis of Figs. 9 and 10 corresponds to the value of N_{obs} used for testing. In the case of the DNN estimators, the weights and biases were initialized to those used in Figs. 7 and 8 (transfer learning). Overall, when $N_{\text{obs}} = 50$, the performance

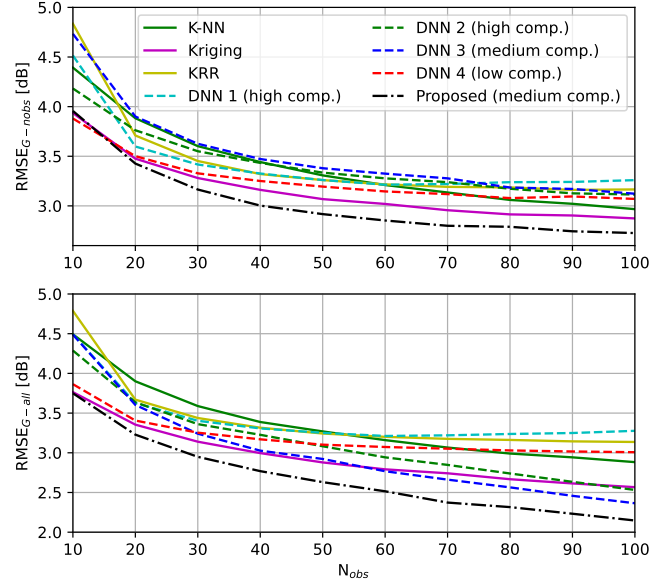


Fig. 10: Grid-aware performance metrics for USRP data vs. the number of observations when $L = 19.2$ m, $\Delta = 1.2$, and the estimators are trained with $N_{\text{obs}} = 50$. The weights of the DNNs are initialized with the weights obtained from training the DNNs with $N_{\text{obs}} \in [10, 100]$.

metrics in Fig. 10 are lower than in Fig. 8. In principle, one would expect that the performance be degraded when N_{obs} is away from 50. However, this effect is not clearly manifest in Figs. 9 and 10, which suggests that for the USRP dataset, the performance of the estimators is not highly sensitive to the value of N_{obs} used during training. However, it will be seen later that this is not the case for the 4G dataset.

The previous two experiments adopted a patch size of $L = 19.2$ m, which resulted in 16×16 grids. To assess performance for larger grids, the patch size is next increased to $L = 38.4$ m, which results in an area of $1,475$ m² and 32×32 grids. The number of significantly distinct training and testing patches is now smaller, so the results are slightly less reliable.

Figs. 11 and 12 show the four metrics when the estimators were trained by selecting N_{obs} uniformly at random in $[40, 150]$. For a given N_{obs} , the error metrics are significantly larger than in Figs. 7 and 8. This is due to two effects. First, the spatial density of measurements is now 4 times smaller. This affects both non-DNN and DNN estimators. It also implies that each additional measurement entails a smaller reduction in the estimation error, as can be seen by the smaller slope of the curves in Figs. 11 and 12 compared to Figs. 7 and 8. Second, the number of significantly distinct training patches is now smaller, which reduces the amount of information in the training dataset. This affects mainly DNN estimators.

The proposed hybrid algorithm outperforms the other estimators by a much wider margin than in Figs. 7 and 8 because its reliance on traditional estimators renders it less sensitive to the amount of information in the training data. Observe, e.g., that the proposed algorithm requires 90 measurements less than the best competitor to attain $\text{RMSE}_{\text{G-all}} \approx 3$ dB.

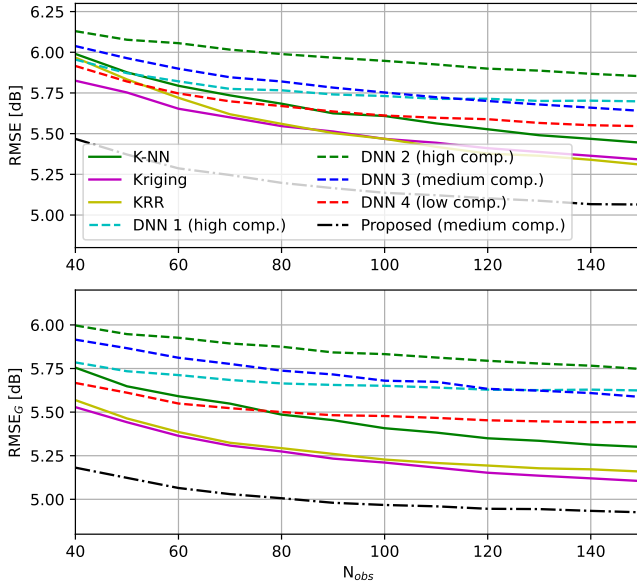


Fig. 11: Grid-agnostic performance metrics for USRP data vs. the number of observations when $L = 38.4$ m, $\Delta = 1.2$, and the estimators are trained with $N_{\text{obs}} \in [40, 150]$.

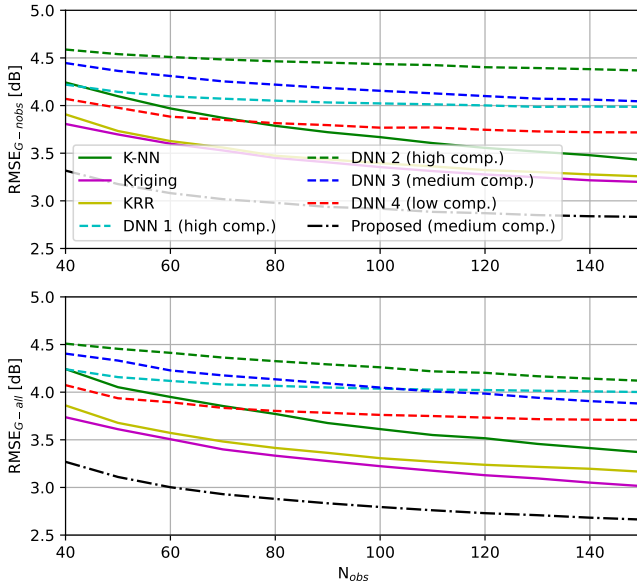


Fig. 12: Grid-aware performance metrics for USRP data vs. the number of observations when $L = 38.4$ m, $\Delta = 1.2$, and the estimators are trained with $N_{\text{obs}} \in [40, 150]$.

Interestingly, DNN 1 and DNN 4, based on autoencoders, outperform the rest of DNNs, suggesting that this architecture is especially useful when the amount of training data is small.

In view of the above experiments, one may wonder whether the good performance of non-DNN estimators relative to DNN estimators is a consequence of the limited amount of training data. In other words, whether the size of the USRP dataset is sufficient for this study. To investigate this, Fig. 13 depicts the $\text{RMSE}_{\text{G-all}}$ vs. the number of measurement sets

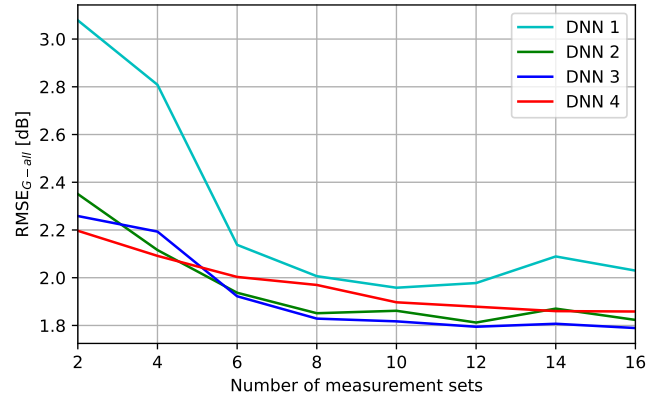


Fig. 13: RMSE for USRP data vs. the number of datasets used during training for the compared DNNs when $L = 19.2$ m, $\Delta = 1.2$, and $N_{\text{obs}} = 30$.

used for training each DNN estimator when $N_{\text{obs}} = 30$ and $L = 19.2$ m. Specifically, for each point in the x-axis, the DNN estimators were trained with the first measurement sets and tested on the last two measurement sets. At each point, the DNN weights are initialized using the weights obtained using the preceding number of measurement sets.

Fig. 13 demonstrates that $\text{RMSE}_{\text{G-all}}$ reaches a plateau when the number of measurement sets used for training is around 10. This suggests that the quantity of USRP data collected is sufficient to train the considered DNN estimators and to enable a fair comparison between non-DNN and DNN estimators. In other words, additional training data beyond this point is not expected to alter the comparisons and observations in the previous experiments.

D. Monte Carlo Experiments with 4G Data

In the case of the 4G data set, recall that there is a measurement set for every cell in two different geographic areas.

Due to space limitations, only one of the measured metrics will be considered, namely RSRP. The reason for selecting this metric is its greater repeatability, which is a consequence of its lower sensitivity to interference. To corroborate this fact, Fig. 14 shows the histograms of the difference between each measurement and the sample mean of the measurements associated with the same grid point. It is indeed observed that the variance of RSRP is the smallest among the three metrics, which also suggests that RSRP is the most suitable for RME.

Since most of the cells are measured only in a small fraction of the $\underline{N}_x \underline{N}_y$ locations, the cell with most measurements is selected in the first area and the two cells with most measurements are selected in the second one. This results in three measurement sets, two of them used for training and the third used for testing. The selected cells operate in LTE bands 7 and 20. A total of 30,000 estimation instances are formed by first choosing a training measurement set uniformly at random and then randomly choosing a patch; cf. Sec. IV. Each of these estimation instances is partitioned into an observed and

TABLE II: Table summarizing the relative performance of the estimators in the literature. The proposed hybrid estimator is excluded from the comparison since it outperforms existing estimators in most cases.

Estimators	Strengths/Limitations	Best Performance Cases			
		Metric	#Meas.	Dataset	$N_y \times N_x$
K-NN	Strengths: 1) Simple and easy to implement. 2) Requires a small amount of training data. Limitations: 1) Limited ability to capture complex spatial patterns.	RMSE _{G-nobs}	High	USRP, $N_{\text{obs}} \in [10, 100]$	16×16
		RMSE _{G-nobs}	Low	4G Data, $N_{\text{obs}} \in [10, 100]$	16×16
		RMSE _{G-all}	Low	4G Data, $N_{\text{obs}} \in [10, 100]$	16×16
Kriging	Strengths: 1) Requires a small amount of training data. 2) Offers uncertainty estimates for predictions. Limitations: 1) Computationally intensive for large N_{obs} due to matrix inversion.	RMSE _{G-nobs}	Low	USRP, $N_{\text{obs}} \in [10, 100]$	16×16
		RMSE	High	USRP, $N_{\text{obs}} \in [10, 100]$	16×16
		RMSE _G	High	USRP, $N_{\text{obs}} \in [10, 100]$	16×16
		RMSE _{G-nobs}	High	USRP, $N_{\text{obs}} = 50$	16×16
		RMSE	High	USRP, $N_{\text{obs}} = 50$	16×16
		RMSE _G	High	USRP, $N_{\text{obs}} = 50$	16×16
		RMSE _{G-all}	Low	USRP, $N_{\text{obs}} = 50$	16×16
		RMSE _{G-nobs}	All	USRP, $N_{\text{obs}} \in [40, 150]$	32×32
		RMSE _{G-all}	All	USRP, $N_{\text{obs}} \in [40, 150]$	32×32
		RMSE	Low	USRP, $N_{\text{obs}} \in [40, 150]$	32×32
		RMSE _G	All	USRP, $N_{\text{obs}} \in [40, 150]$	32×32
		RMSE	High	4G Data, $N_{\text{obs}} \in [10, 100]$	16×16
KRR	Strengths: 1) Requires a small amount of training data. 2) Theoretical performance guarantees [22]. Limitations: 1) Computationally intensive for large N_{obs} due to matrix inversion.	RMSE	High	USRP, $N_{\text{obs}} \in [40, 150]$	32×32
DNN 1	Strengths: 1) Provides uncertainty metrics to enable active sensing [19]. Limitations: 1) Computationally expensive due to the large number of parameters.	RMSE	Low	USRP, $N_{\text{obs}} \in [10, 100]$	16×16
DNN 2	Strengths: 1) Ability to capture complex patterns if sufficient data is given. Limitations: 1) More trainable parameters than other DNN estimators.	RMSE _{G-nobs}	High	4G Data, $N_{\text{obs}} \in [10, 100]$	16×16
		RMSE _G	High	4G Data, $N_{\text{obs}} \in [10, 100]$	16×16
DNN 3	Strengths: 1) Ability to capture complex patterns if sufficient data is given. 2) Provides uncertainty metrics to enable active sensing. 3) Similar overall performance to DNN 2 with a smaller number of parameters. Limitations: 1) More trainable parameters than DNN 4.	RMSE _{G-all}	High	USRP, $N_{\text{obs}} \in [10, 100]$	16×16
		RMSE _{G-all}	High	USRP, $N_{\text{obs}} = 50$	16×16
DNN 4	Strengths: 1) Lowest complexity among all DNN estimators. 2) Strong performance when the amount of training data or observations is low. Limitations: 1) Performance may be sensitive to the value of N_{obs} used for training.	RMSE _G	Low	USRP, $N_{\text{obs}} \in [10, 100]$	16×16
		RMSE _{G-all}	Low	USRP, $N_{\text{obs}} \in [10, 100]$	16×16
		RMSE	Low	USRP, $N_{\text{obs}} = 50$	16×16
		RMSE _G	Low	USRP, $N_{\text{obs}} = 50$	16×16
		RMSE	Low	4G Data, $N_{\text{obs}} \in [10, 100]$	16×16
		RMSE _G	Low	4G Data, $N_{\text{obs}} \in [10, 100]$	16×16

an unobserved set 5 times as described in Sec. V-B2, resulting in a total of 150,000 training examples.

Figs. 15 and 16 depict the performance metrics when the patch side is $L = 64$ m, which results in an area of 4096 m² and $N_x = N_y = L/\Delta = 16$. In general, the performance metrics are significantly lower than in the USRP dataset. The reason is that the transmitters in the 4G dataset are farther away from the mapped region and therefore the true maps exhibit a smaller variability. This is consistent with the theoretical findings in [5]. It also agrees with the fact that the performance of K-NN is less sensitive to N_{obs} in the 4G dataset than in the USRP dataset.

Observe that RMSE_G is higher than RMSE. To understand this effect, recall that to collect this dataset 5 measurements were acquired while the UAV was hovering at each grid point. Thus, the selection of the observed measurements used for RMSE_G (cf. Sec. V-B) yields very accurate information of the true map at a small number of grid points, whereas in the case of RMSE, the information is less accurate but comprises a larger number of grid points. In view of Fig. 15, the benefit

of a larger number of grid points dominates. This could not be the case if the measurement error were higher. The grid-aware metrics take lower values than the grid-agnostic RMSE in part also because the measurements were acquired at the grid points. This means that for a given N_{obs} , the number of actual observations is 5 times greater in the case of RMSE.

For all four metrics, the proposed hybrid estimator outperforms the rest, which demonstrates once more the importance of combining DNN and non-DNN estimators. Remarkably, Kriging is outperformed by some DNN estimators in 3 out of the 4 metrics. In the case of K-NN, RMSE_G is poor because most neighbors are selected from the same grid point, which reduces the spatial resolution of its estimates. Averaging nearby measurements may be a desirable pre-processing step when applying this algorithm. This is further corroborated by the remarkably good values that this estimator achieves for the grid-aware metrics when N_{obs} is low.

As in Sec. V-C, it is worth investigating whether performance may improve if the estimator parameters are set depending on N_{obs} . To this end, Figs. 17 and 18 were obtained

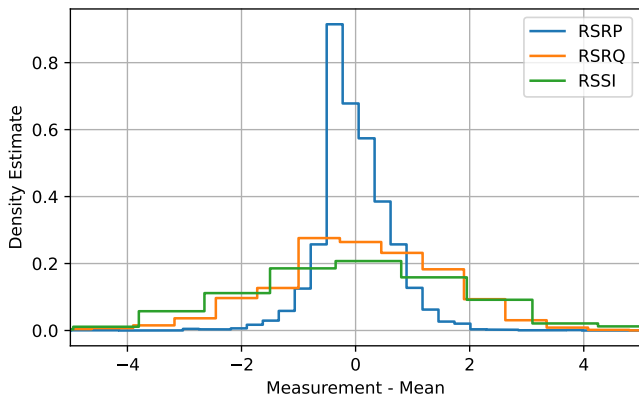


Fig. 14: Histogram plots of the difference between measurements associated with the (i, j) -th grid point and their mean for different metrics of one of the 4G measurement sets per metric.

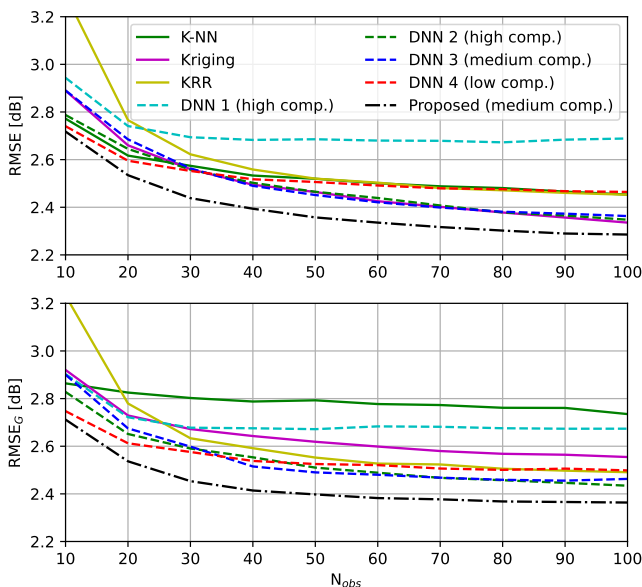


Fig. 15: Grid-agnostic performance metrics for 4G data vs. the number of observations when $L = 64$ m, $\Delta = 4$, and the estimators are trained with $N_{\text{obs}} \in [10, 100]$.

by repeating the experiment in Figs. 15 and 16 with all estimators trained for $N_{\text{obs}} = 50$. The weights of the DNN estimators were initialized to those obtained for Figs. 15 and 16. It is observed that training specifically for $N_{\text{obs}} = 50$ generally improves the performance metrics at $N_{\text{obs}} = 50$ while they become degraded away from this value. This effect is more manifest than in the case of the USRP dataset. However, different algorithms exhibit a markedly different sensitivity to the value of N_{obs} used for training. For instance, K-NN and Kriging are only slightly affected by this parameter. In the case of other estimators, such as those based on autoencoders (DNN1 and DNN4) and the proposed hybrid estimator, the metrics improve slightly at $N_{\text{obs}} = 50$ but they are significantly degraded away from this value. Thus,

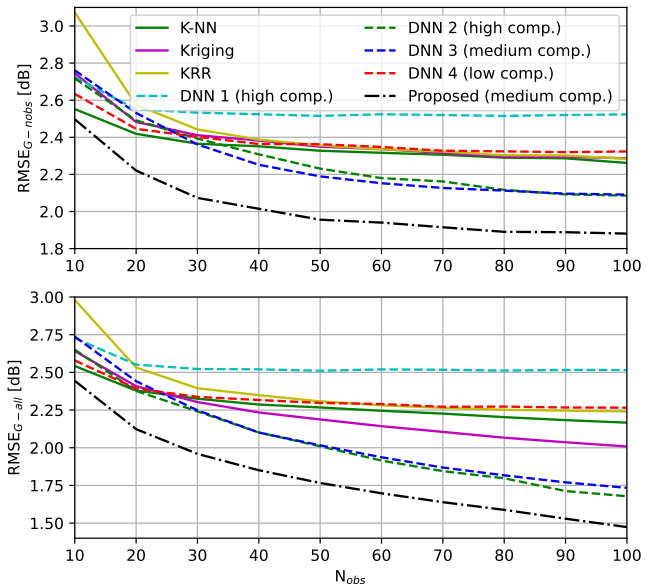


Fig. 16: Grid-aware performance metrics for 4G data vs. the number of observations when $L = 64$ m, $\Delta = 4$, and the estimators are trained with $N_{\text{obs}} \in [10, 100]$.

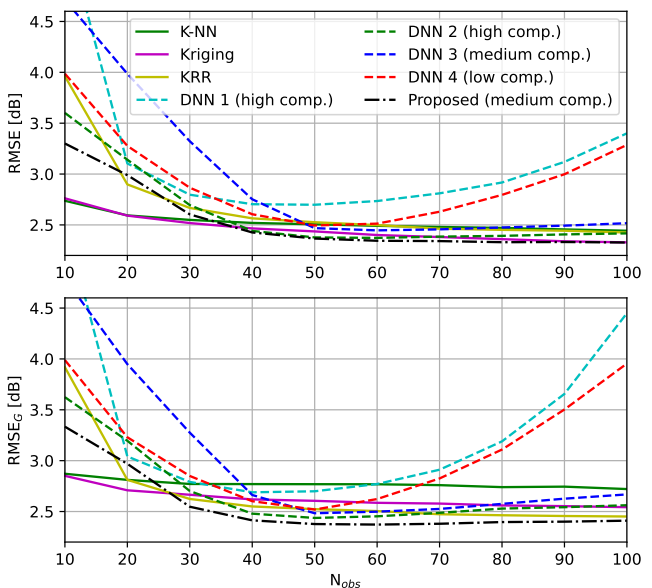


Fig. 17: Grid-agnostic performance metrics for 4G data vs. the number of observations when $L = 64$ m, $\Delta = 4$, and the estimators are trained with $N_{\text{obs}} = 50$ for 4G data. The weights of the DNNs are initialized with the weights obtained from training the DNNs with $N_{\text{obs}} \in [10, 100]$.

for all these estimators, it may not be worth using different parameter values depending on N_{obs} . On the contrary, for estimators such as DNN2 and DNN3, based on U-Nets, the metrics improve significantly at $N_{\text{obs}} = 50$, which means that it may be convenient in practice to use different weights and biases depending on N_{obs} .

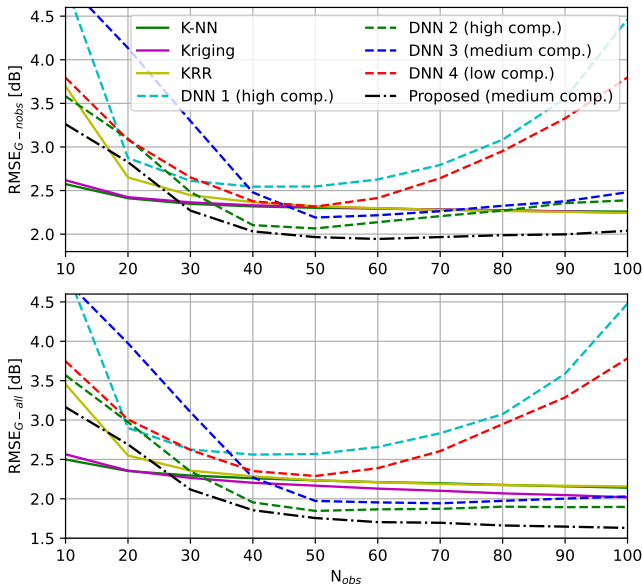


Fig. 18: Grid-aware performance metrics for 4G data vs. the number of observations when $L = 64$ m, $\Delta = 4$, and the estimators are trained with $N_{\text{obs}} = 50$ for 4G data. The weights of the DNNs are initialized with the weights obtained from training the DNNs with $N_{\text{obs}} \in [10, 100]$.

VI. CLOSING REMARKS

A. Summary of the Key Observations

The main findings from the experiments in Sec. V are summarized next:

- 1) The overall estimation error is reasonably small in most scenarios for a relatively small number of measurements, which suggests that the estimated maps may be sufficiently accurate for real-world applications and, therefore, constitutes empirical evidence for the practical relevance of RME.
- 2) Grid-aware metrics are typically lower than grid-agnostic metrics, which suggests that averaging out small-scale fading is beneficial for RME.
- 3) Averaging the measurements assigned to a gridpoint $\mathbf{x}_{i,j}^G$ in dB units to obtain the grid-quantized measurement $\tilde{\gamma}_{i,j}$ seems to be the most effective approach to average out small-scale fading among the considered alternatives; cf. Sec. IV-A3.
- 4) The overall error depends on the spatial variability of the maps. If the transmitters are farther away from the mapped region, as occurs in the 4G dataset, a smaller error must be expected. This is consistent with the theoretical findings in [5].
- 5) Among the estimators in the literature, no one outperforms the others in all scenarios. Each one exhibits the best performance in certain situations, as summarized in Table II.
- 6) Traditional estimators exhibit noteworthy good performance. This fact may have gone unnoticed in a large part of the literature, where sophisticated estimators are proposed but not compared with simple benchmarks. The

simple Kriging algorithm, for example, proved highly versatile with top performance in a wide variety of cases, which provides further empirical evidence for the correlated shadow fading model in [31].

- 7) The proposed hybrid estimator, which was designed to combine the merits of existing algorithms at the expense of a greater computational burden than some DNN estimators, is indeed observed to outperform all existing estimators in nearly all cases.
- 8) Traditional estimators exhibit a highly competitive performance especially when the amount of training data is not sufficiently large. Even when there is sufficient training data, performance gains due to the usage of DNN-based estimators is most often of a fraction of a dB. Besides, as observed in Sec. V-C (see also Sec. IV), large patch sizes greatly increase the amount of data that must be collected to train DNN estimators, which renders traditional estimators more appealing for large areas.
- 9) Autoencoder-based architectures prove to be particularly well-suited for situations characterized by a low number of measurements or limited training data. In turn, U-Net architectures tend to manifest superior performance in instances where sufficient training data is available and a substantial number of measurements (N_{obs}) is given.
- 10) As observed by the comparison between RMSE and RMSE_G , some estimators are more sensitive to whether the measurements are more clustered at a small set of locations or more uniformly spread across the area.
- 11) Depending on the dataset and estimator, it may be worth using different parameter values depending on the number of observations (N_{obs}).
- 12) RSRP is more suitable than RSRQ and RSSI for RME due to its greater repeatability.

B. Discussion

As with any empirical study, the work at hand features strengths and limitations. Within the strengths, one can highlight the following: (i) The collected dataset is significantly larger than in all previous works and comprises multiple frequency bands, especially in the context of cellular communications. (ii) A wide range of existing estimators were compared. Most of them had never been compared with each other. (iii) The four considered performance metrics are useful to capture the needs of a wide variety of applications and illustrate different effects and trade-offs in RME.

Among the limitations of the study, it is worth mentioning the following: (i) Only estimation of power maps was considered. Different kinds of radio maps (see e.g. [1]) will require separate studies. (ii) Although the collected data spans a significant collection of practically relevant scenarios, new data must be collected for empirically analyzing estimators in other setups, such as those involving higher frequency bands (e.g. mmWave bands), urban scenarios, user mobility, and terminals that are closer to the ground. (iii) Although a representative set of existing estimators was considered, many other estimators in the literature were not analyzed here. To allow researchers to assess the performance of those

estimators, our datasets and code will be published. (iv) Although the heading of the UAV was kept constant to reduce the impact of antenna directivity, it is still present to some extent in the measurements. Compensating for this effect is left for future work.

C. Conclusions

The present work addressed a knowledge gap in the literature by testing a representative subset of radio map estimators on real data. To analyze the impact of small-scale fading, two formulations of the RME problem were considered. Two large datasets were collected with two different measurement systems, one of them specifically developed for this work. Performance was evaluated using four different metrics and a large number of general observations were drawn from the experiments and summarized in Sec. VI-A.

The selection of an estimator depends on the available computational resources and the specific characteristics of the data, such as the number of measurements, spatial variability of the true map, and the dimensions of the mapped area. The present work aims at providing a useful guide to accomplish this decision in a wide variety of scenarios; cf. Table II.

Finally, an estimator that combines the merits of traditional and DNN-based algorithms was proposed and it was seen to consistently outperform existing methods in the majority of cases. This opens the door to devising further estimators of this kind.

Future directions will address the limitations listed in Sec. VI-B and on developing further hybrid estimators.

REFERENCES

- [1] D. Romero and S.-J. Kim, "Radio map estimation: A data-driven approach to spectrum cartography," *IEEE Signal Process. Mag.*, vol. 39, no. 6, pp. 53–72, 2022.
- [2] A. Alaya-Feki, S. B. Jemaa, B. Sayrac, P. Houze, and E. Moulines, "Informed spectrum usage in cognitive radio networks: Interference cartography," in *Proc. IEEE Int. Symp. Personal, Indoor Mobile Radio Commun.*, Cannes, France, Sep. 2008, pp. 1–5.
- [3] M. Höyhtyä, A. Mämmelä, M. Eskola, M. Matinmikko, J. Kalliovaara, J. Ojaniemi, J. Suutala, R. Ekman, R. Bacchus, and D. Roberson, "Spectrum occupancy measurements: A survey and use of interference maps," *IEEE Commun. Surveys Tutorials*, vol. 18, no. 4, pp. 2386–2414, 2016.
- [4] M. Pesko, T. Javornik, A. Kosir, M. Stular, and M. Mohorcic, "Radio environment maps: The survey of construction methods," *KSII Trans. Internet Information Systems*, vol. 8, no. 11, pp. 3789–3809, 2014.
- [5] D. Romero, T. N. Ha, R. Shrestha, and M. Franceschetti, "Theoretical analysis of the radio map estimation problem," 2023.
- [6] R. Shrestha, T. N. Ha, P. Q. Viet, and D. Romero, "Radio map estimation in the real-world: Empirical validation and analysis," in *2023 IEEE Conf. on Antenna Measurements and Appl. (CAMA)*, Genoa, Italy, 2023, pp. 169–174.
- [7] Z. El-friakh, A. M. Voicu, S. Shabani, L. Simić, and P. Mähönen, "Crowdsourced indoor Wi-Fi REMs: Does the spatial interpolation method matter?," in *2018 IEEE Int. Symp. Dynamic Spectrum Access Netw.* IEEE, 2018, pp. 1–10.
- [8] Z. Xiang, H. Zhang, J. Huang, S. Song, and K.C. Almeroth, "A hidden environment model for constructing indoor radio maps," in *IEEE Int. Symp. World Wireless Mobile Multimedia Net.*, 2005, pp. 395–400.
- [9] Y. Hu, W. Zhou, Z. Wen, Y. Sun, and B. Yin, "Efficient radio map construction based on low-rank approximation for indoor positioning," *Math. Probl. Eng.*, vol. 2013, 2013.
- [10] B. Yang, S. He, and S.-H. G. Chan, "Updating wireless signal map with Bayesian compressive sensing," in *Proc. ACM Int. Conf. Mod., Anal. and Simu. Wireless and Mobile Sys.*, New York, NY, USA, 2016, MSWiM '16, pp. 310–317, Association for Computing Machinery.
- [11] Q. Niu, Y. Nie, S. He, N. Liu, and X. Luo, "RecNet: A convolutional network for efficient radiomap reconstruction," in *IEEE Int. Conf. Commun.*, 2018, pp. 1–7.
- [12] M. Iwasaki, T. Nishio, M. Morikura, and K. Yamamoto, "Transfer learning-based received power prediction with ray-tracing simulation and small amount of measurement data," *arXiv preprint arXiv:2005.00833*, 2020.
- [13] C. Parera, Q. Liao, I. Malanchini, C. Tatino, A. E. C. Redondi, and M. Cesana, "Transfer learning for tilt-dependent radio map prediction," *IEEE Trans. Cognitive Commun. Netw.*, vol. 6, no. 2, pp. 829–843, Jan. 2020.
- [14] T. Hayashi, T. Nagao, and S. Ito, "A study on the variety and size of input data for radio propagation prediction using a deep neural network," in *Proc. IEEE European Conf. Antennas Propag.*, Copenhagen, Denmark, Jul. 2020, IEEE, pp. 1–5.
- [15] E. Ostlin, H.-J. Zepernick, and H. Suzuki, "Macrocell path-loss prediction using artificial neural networks," *IEEE Trans. on Veh. Technol.*, vol. 59, no. 6, pp. 2735–2747, 2010.
- [16] S. I. Popoola, A. Jefia, A. A. Atayero, O. Kingsley, N. Faruk, O. F. Oseni, and R. O. Abolade, "Determination of neural network parameters for path loss prediction in very high frequency wireless channel," *IEEE Access*, vol. 7, pp. 150462–150483, 2019.
- [17] W.C.M.V. Beers and J.P.C. Kleijnen, "Kriging interpolation in simulation: A survey," in *Proc. IEEE Winter Simulation Conf.*, Washington, D. C., Dec. 2004, vol. 1, pp. 113–121.
- [18] A. Agarwal and R. Gangopadhyay, "Predictive spectrum occupancy probability-based spatio-temporal dynamic channel allocation map for future cognitive wireless networks," *Trans. Emerging Telecommun. Technol.*, vol. 29, no. 8, pp. e3442, 2018.
- [19] R. Shrestha, D. Romero, and S. P. Chepuri, "Spectrum surveying: Active radio map estimation with autonomous UAVs," *IEEE Trans. Wireless Commun.*, vol. 22, no. 1, pp. 627–641, 2022.
- [20] G. Boccolini, G. Hernandez-Penalzoa, and B. Beferull-Lozano, "Wireless sensor network for spectrum cartography based on kriging interpolation," in *Proc. IEEE Int. Symp. Personal, Indoor Mobile Radio Commun.*, Sydney, NSW, Nov. 2012, pp. 1565–1570.
- [21] B. Schölkopf and A. J. Smola, *Learning with Kernels: Support Vector Machines, Regularization, Optimization, and Beyond*, MIT Press, 2002.
- [22] D. Romero, S.-J. Kim, G. B. Giannakis, and R. López-Valcarce, "Learning power spectrum maps from quantized power measurements," *IEEE Trans. Signal Process.*, vol. 65, no. 10, pp. 2547–2560, May 2017.
- [23] T. Imai, K. Kitao, and M. Inomata, "Radio propagation prediction model using convolutional neural networks by deep learning," in *Proc. IEEE European Conf. Antennas Propag.*, Krakow, Poland, Apr. 2019, IEEE, pp. 1–5.
- [24] Y. Teganya and D. Romero, "Deep completion autoencoders for radio map estimation," *IEEE Trans. Wireless Commun.*, vol. 21, no. 3, pp. 1710–1724, 2021.
- [25] E. Krijestorac, S. Hanna, and D. Cabric, "Spatial signal strength prediction using 3D maps and deep learning," in *Proc. IEEE Int. Conf. Commun.* IEEE, 2021, pp. 1–6.
- [26] J. Thrane, D. Zibar, and H. L. Christiansen, "Model-aided deep learning method for path loss prediction in mobile communication systems at 2.6 GHz," *IEEE Access*, vol. 8, pp. 7925–7936, 2020.
- [27] V. V. Ratnam, H. Chen, S. Pawar, B. Zhang, C. J. Zhang, Y.-J. Kim, S. Lee, M. Cho, and S.-R. Yoon, "FadeNet: Deep learning-based mm-wave large-scale channel fading prediction and its applications," *IEEE Access*, vol. 9, pp. 3278–3290, 2020.
- [28] R. Levie, Ç. Yapar, G. Kutyniok, and G. Caire, "RadioUNet: Fast radio map estimation with convolutional neural networks," *IEEE Trans. Wireless Commun.*, vol. 20, no. 6, pp. 4001–4015, 2021.
- [29] X. Han, L. Xue, F. Shao, and Y. Xu, "A power spectrum maps estimation algorithm based on generative adversarial networks for underlay cognitive radio networks," *Sensors*, vol. 20, no. 1, pp. 311, Jan. 2020.
- [30] S. Shrestha, X. Fu, and M. Hong, "Deep generative model learning for blind spectrum cartography with NMF-based radio map disaggregation," in *Proc. IEEE Int. Conf. Acoust., Speech, Signal Process.* IEEE, 2021, pp. 4920–4924.
- [31] M. Gudmundson, "Correlation model for shadow fading in mobile radio systems," *Electron. Letters*, vol. 27, no. 23, pp. 2145–2146, Nov. 1991.